ELSEVIER

Nuclear Instruments and Methods in Physics Research A 411 (1998) 63–74

NUCLEAR INSTRUMENTS & METHODS IN PHYSICS RESEARCH Section A

Performance of the NOMAD transition radiation detector

G. Bassompierre[a], S. Bunyatov[b], T. Fazio[a], J.-M. Gaillard[a], M. Gouanère[a], E. Manola-Poggioli[a,1], L. Mossuz[a], J.-P. Mendiburu[a], P. Nédélec[a,1], Yu. Nefedov[b], H. Pessard[a], D. Sillou[a,*], V. Valuev[a,b,1], D. Verkindt[a]

[a] *Laboratoire d'Annecy-le-Vieux de Physique des Particules (LAPP), IN2P3-CNRS, BP 110, F-74019 Annecy-le-Vieux Cedex, France*
[b] *Joint Institute for Nuclear Research (JINR), 141980 Dubna, Moscow Region, Russian Federation*

Received 23 July 1997

Abstract

The NOMAD experiment includes a transition radiation detector that provides a 10^3 pion rejection factor, for a 90% electron identification efficiency. Such a rejection factor is required in the search for $\nu_\mu \to \nu_\tau$ oscillations in the τ electron decay channel and in the search for $\nu_\mu \to \nu_e$ oscillations. Algorithms used for the electron–pion discrimination and results obtained on the data are described.

PACS: 29.40.Ym; 14.60.Cd; 07.85.Yk

Keywords: Transition radiation; Electron identification; Pion rejection; Neutrino oscillations

1. Introduction

The NOMAD experiment [1,2] searches for ν_τ appearing from $\nu_\mu \to \nu_\tau$ oscillations in the CERN SPS wide band neutrino beam, which consists primarily of ν_μ neutrinos with a small ν_e component (less than $\sim 1\%$) and a negligible ($\sim 5 \times 10^{-6}$) contamination of prompt ν_τ [3]. If $\nu_\mu \to \nu_\tau$ oscillations occur, ν_τ would be detected via their charged current (CC) interactions $\nu_\tau + N \to \tau^- + X$ in an active target using the kinematical characteristics of the subsequent τ^- decays.

The electronic decay mode $\tau^- \to e^- \bar{\nu}_e \nu_\tau$ (branching ratio 17.8%) is very promising for τ^- identification. The background due to electrons which originate from ν_e CC interactions ($\nu_e + N \to e^- + X$) or from Dalitz pairs and photon conversions is rejected using kinematic criteria, based on momentum balance in the transverse plane and on particle isolation. However, these kinematical cuts do not eliminate the background from ν_μ neutral current interactions, in which an isolated pion track fakes an electron. To reject this background, as well as for the $\nu_\mu \to \nu_e$ oscillation search, excellent electron identification is required and the overall π rejection achieved by the NOMAD detectors

* Corresponding author. Tel.: (+33) 04 50 09 16 00; fax: (+33) 04 50 27 94 95; e-mail: sillou@lapp.in2p3.fr.

[1] Now at European Organization for Nuclear Research (CERN), CH-1211 Geneva 23, Switzerland.

0168-9002/98/$19.00
PII: S0168-9002(98)00105-3

has to be larger than 10^5. A major part of the electron identification is performed by the transition radiation detector (TRD), which was designed to discriminate between isolated electron and pion tracks with a rejection factor greater than 10^3 for a 90% electron efficiency in a 1–50 GeV/c momentum range.

In this paper we describe the algorithms developed for electron-pion discrimination by the NOMAD TRD and their performance. We review the design of the TRD and the principles of the electron identification in Sections 2 and 3. The algorithms developed for the recognition of electrons are described in Section 4 and discussed in Section 5. The identification performance obtained on the data are described in Section 6.

2. Design of the NOMAD TRD

A detailed description of the NOMAD TRD can be found elsewhere [4]. The design of the detector was optimised using a complete simulation cross-checked with a series of test beam measurements [5]. It also had to satisfy two experimental constraints: the limited longitudinal space available inside the NOMAD magnet and the requirement that there be less than 2% of a radiation length between two consecutive drift chambers.

The detector is located after the NOMAD drift chamber target (see Fig. 1a) and consists of 9 identical modules. The first 8 modules are paired into 4 doublets. Five drift chambers [6] used for tracking and momentum measurements are imbedded in

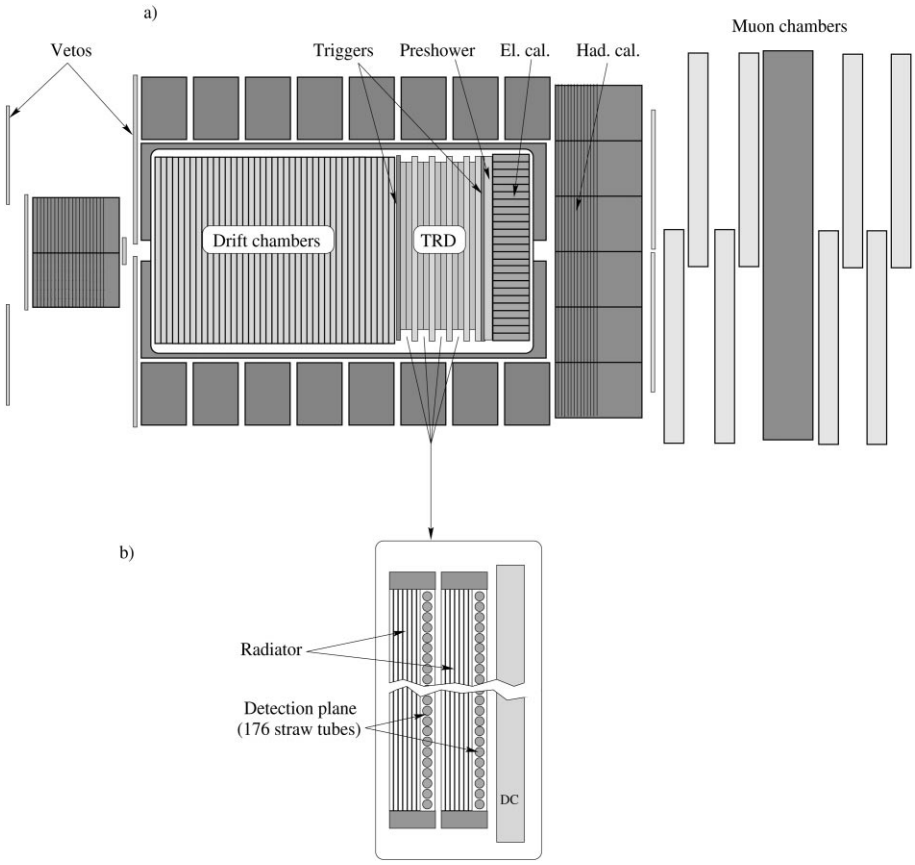

Fig. 1. (a) A topview of the NOMAD detector and (b) a schematic view of a TRD doublet.

the TRD, one after each doublet and one after the last module, in order to provide an accurate track extrapolation from the target to the electromagnetic calorimeter.

Each TRD module comprises a radiator followed by a detection plane (Fig. 1b):

- The radiator is a set of 315 polypropylene foils, each 15 μm thick and $2.85 \times 2.85\,m^2$ in area, separated by 250 μm nitrogen gaps.
- The detection plane consists of 176 vertical straw tubes, each 3 m long and 16 mm in diameter, positioned with a 16.2 mm pitch. The straw tubes are fed in parallel with a 80% xenon-20% methane gas mixture.

The number of modules and the large effective area of a module make the NOMAD TRD one of the largest transition radiation detectors ever built.

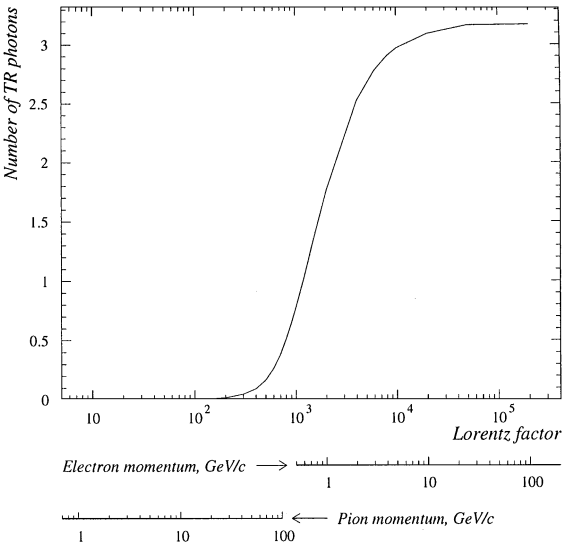

Fig. 2. The number of transition radiation photons emitted by a NOMAD TRD radiator as a function of the Lorentz factor.

3. Principles of TRD electron identification

The theory of transition radiation is well known [7] and numerous detectors using this effect for particle identification have been built [8].

Particle identification by the TRD is based on the difference in the total energy deposited in the detection planes by particles with different Lorentz factors ($\gamma = E/m$). All charged particles crossing the detector lose energy by ionization. In addition, highly relativistic ones (mainly electrons in NOMAD) produce transition radiation (TR) X-rays at the interfaces of the radiator foils.

The number of transition radiation photons emitted by a NOMAD radiator as a function of the Lorentz factor is shown in Fig. 2. As an example, a 10 GeV/c electron at normal incidence emits, on the average, $\simeq 3.1$ photons with a mean energy $\simeq 14$ keV each. About 50% of the photons emitted by a radiator are absorbed in the subsequent detection plane. The average energy of a detected photon is $\simeq 8$ keV, due to the xenon photo-absorption cross-section peak at around 5.5 keV [9]. The energy of the detected TR photons is added to the ionization losses of the parent electron ($\simeq 9$ keV at 10 GeV/c) in the same straw tube, since the photons are emitted at a small mean angle $1/\gamma < 1$ mrad with respect to the electron direction. The 20 keV total average energy deposited by a 10 GeV/c electron is large compared to the mean $\simeq 7.5$ keV energy deposition of a pion of the same momentum. Monte Carlo simulated spectra of the energy deposited by 10 GeV/c electrons and pions are shown in Fig. 3.

4. Electron identification algorithms

The TRD data acquisition and calibration procedures are described in [4]. The signal processing produces a list of TRD hits (straw tubes with an energy deposition above threshold).

The first step of the identification procedure consists in matching the TRD hits with the tracks reconstructed by the drift chambers. As a result, a set of hits collected along the road of a drift chamber track is assigned to this track. With at most one hit per TRD module allowed to be matched, up to 9 hits can be associated with a track. The energy depositions in the associated hits are then compared to the expectations for the two particle hypotheses, electron e and pion π, taking into

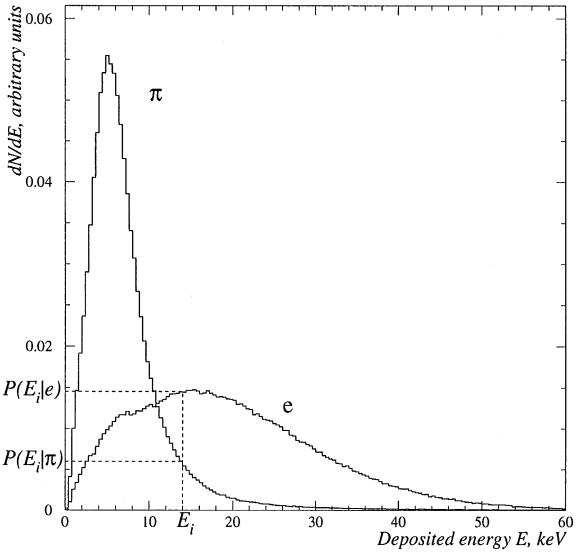

Fig. 3. Normalized spectra of energy deposited in the TRD straw tube gas mixture by 10 GeV/c pions and electrons at normal incidence (Monte Carlo simulation).

account the momentum of the particle as measured by the drift chambers.

Two different identification procedures have been developed for isolated and non-isolated particles and are applied according to the topology of the event:

- If all the hits of the set are associated with a single track, the particle is defined as isolated, Fig. 4a.
- If several particles cross the same straw tubes, their energy depositions are summed up. When such "shared" hits are matched with several tracks, the particle is defined as non-isolated, Fig. 4b.

4.1. Identification of isolated particles

For each track with associated hits in the TRD, a likelihood ratio estimator $\mathscr{L}$ is constructed:

$$\mathscr{L} = \sum_{i=1}^{N_h} \log \frac{P(E_i \mid e)}{P(E_i \mid \pi)}, \quad (1)$$

where N_h is the number of TRD hits associated with a particle; $P(E_i \mid e)$ and $P(E_i \mid \pi)$ are the probability density functions for an electron e and for a pion π to deposit the energy E_i in the ith straw tube (Fig. 3).

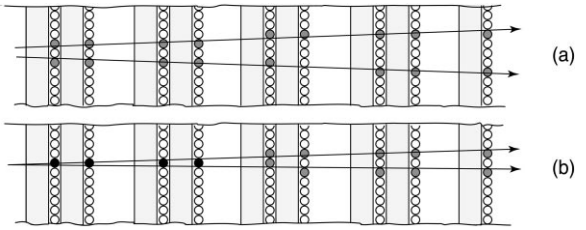

Fig. 4. Examples of different track topologies in TRD (schematic top view): (a) isolated particles, all the associated hits are "non-shared" (shown in grey); (b) non-isolated particles, hits associated in the first 4 modules are "shared" (shown in black).

The probability densities $P(E_i \mid e)$ and $P(E_i \mid \pi)$ are functions of many parameters, such as the particle Lorentz factor, momentum, angles with respect to the straw tube, etc. These functions have been obtained from detailed simulation and extensive test beam measurements and are discussed in the following sections.

Eq. (1) assumes uncorrelated signals in different detection planes. In the case of electrons, a fraction of the transition radiation photons emitted in the first radiator of a doublet may be detected in the second module, leading to a correlation. As discussed in Section 5, this effect can be neglected in the NOMAD TRD setup.

The distributions of the likelihood ratio (1) are computed for the two particle hypotheses (e and π). The fractions of electrons and pions above a certain threshold value $\mathscr{L}_{th}$ define, respectively, the efficiency for electron identification (ε_e) and the corresponding pion acceptance (ε_π), see Fig. 5. Fig. 6, obtained by integration of the likelihood ratio distributions, represents the electron efficiency ε_e and the pion acceptance ε_π as a function of the threshold $\mathscr{L}_{th}$. For each track with N_h associated hits, the decision on the nature of the particle is made by comparing the value of the computed likelihood ratio $\mathscr{L}$ with the threshold $\mathscr{L}_{th}$ for the required values of ε_e or ε_π.

The expected pion acceptance for different electron identification efficiencies is shown as a function of the number of hits in Fig. 7 for 1 GeV/c and 10 GeV/c particles. A minimum number of 4 hits is

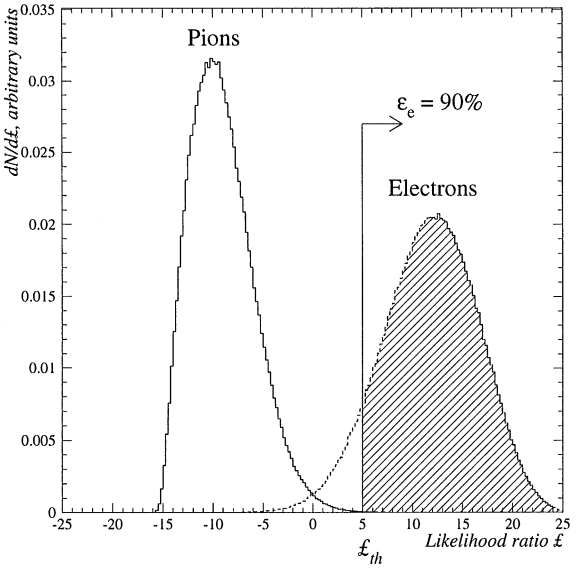

Fig. 5. The likelihood ratio distributions for 10 GeV/c pions and electrons with 9 associated TRD hits (Monte Carlo simulation). A threshold corresponding to a 90% electron identification efficiency is shown.

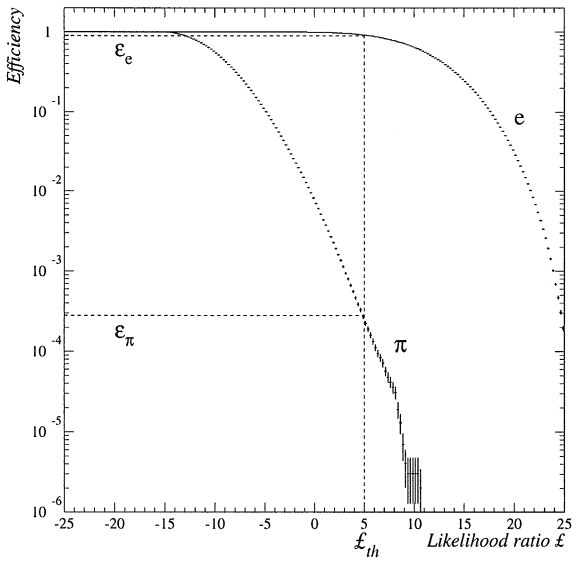

Fig. 6. Electron identification efficiency ε_e and pion acceptance ε_π as a function of the threshold for 10 GeV/c particles with 9 associated hits (Monte Carlo simulation). The threshold value $\mathscr{L}_{th}$ shown corresponds to $\varepsilon_e = 90\%$.

necessary to have a reliable association with a DC track, therefore, we require a signal in at least 4 detection planes to apply the identification algorithm. The pion rejection factor $R = 1/\varepsilon_\pi$ achieved with 9 TRD modules is larger than 10^3 for a 90% electron efficiency.

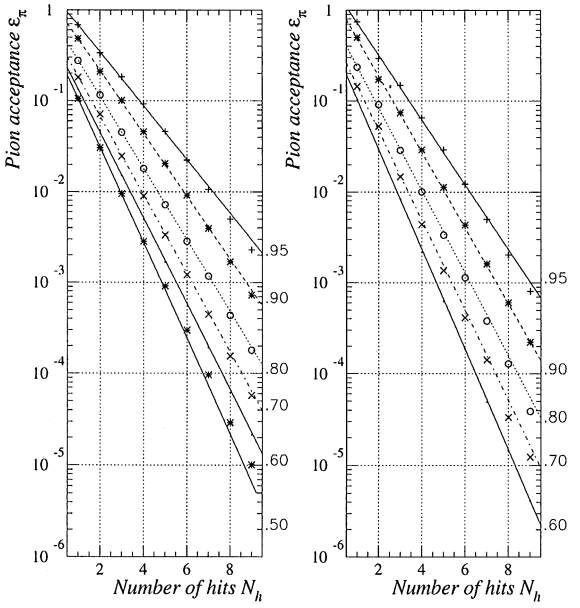

Fig. 7. Expected pion acceptance, ε_π, corresponding to fixed values of electron identification efficiency, ε_e, as a function of the number of associated hits N_h, for 1 GeV/c (left) and 10 GeV/c (right) particles. Straight lines are drawn to guide the eye; points along each line are computed for the value of ε_e indicated at the end of the line, on the right.

The electron efficiency ε_e for a pion acceptance $\varepsilon_\pi = 10^{-3}$ for 9 associated hits as a function of the momentum of the incident particle is shown in Fig. 8. It is larger than 90% in the momentum range from 1 to 50 GeV/c. Below 1 GeV/c, the TRD identification capability degrades rapidly due to the fact that the transition radiation yield for electrons sharply decreases. Above 50 GeV/c, electron-pion discrimination deteriorates because the TR photon production by pions becomes significant (see Fig. 2). In practice, we apply the identification algorithm to particles in the momentum range from 0.5 to 50 GeV/c.

The identification algorithm described above gives a poor rejection for low momentum (below $\sim$1.5 GeV/c) protons due to their large ionization losses. Electron–proton discrimination by TRD in this momentum range requires a dedicated treatment, which will be described elsewhere.

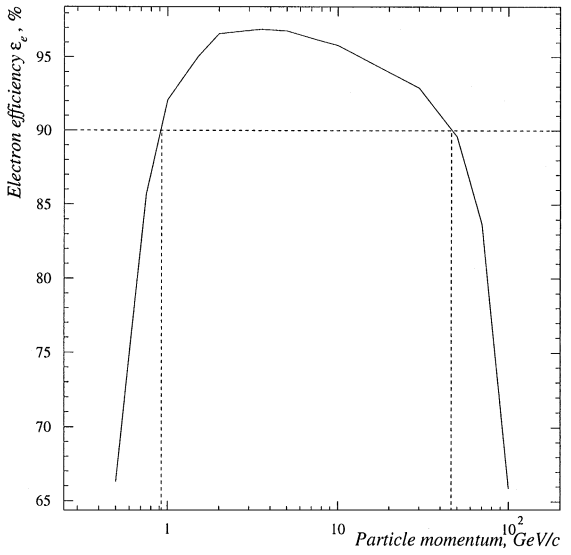

Fig. 8. Monte Carlo predicted electron efficiency ε_e corresponding to $\varepsilon_\pi = 10^{-3}$ as a function of the momentum of the particle for 9 associated hits.

4.2. Identification of non-isolated particles

4.2.1. The method

The main task of the TRD is the identification of electrons produced in τ decays or in ν_e CC interactions which are in general well isolated from other tracks in an event. However, the identification of non-isolated particles by the TRD is also possible (though with smaller efficiency), as the number of tracks producing each TRD hit is known from the accurate reconstruction of the track coordinates in the drift chambers. The identification of non-isolated electrons is useful in processes where an electron is imbedded in the hadron jet (e.g., decays of charmed particles).

Two tracks whose projections onto the horizontal plane are close to one another cannot be separated in the TRD. For instance, in the case of ν_e CC interactions, about 25% of the events include tracks crossing the same straw tubes, producing so-called "shared" hits. Application of the identification algorithm described in the previous section to "shared" hits with the sum of the energies deposited by each of the non-isolated tracks would lead to substantial particle misidentification. For example, more than 95% of the two pions with all 9 hits "shared" would be identified as electrons.

We have developed a procedure for the identification of non-isolated particles which takes into account the number of tracks associated with each hit as well as the particle momenta. This algorithm is applied to a pair of tracks if the number of "shared" hits is larger than 3. If two tracks share less than 4 hits, they are treated separately by the particle identification procedure for isolated tracks (Section 4.1) applied to their "non-shared" hits only.

While for an isolated particle of momentum p the decision is made between the two hypotheses $e(p)$ and $\pi(p)$, for two non-isolated particles of momenta p_1 and p_2 one has to consider four hypotheses $\pi(p_1)*\pi(p_2)$, $e(p_1)*\pi(p_2)$, $\pi(p_1)*e(p_2)$ and $e(p_1)*e(p_2)$. Thus, four likelihood estimators are computed from the corresponding probability density distributions for a combination of two particles:

$$\mathscr{L}_{kl} = \log\left[\prod_{i=1}^{N_{sh}} P(E_i \,|\, k(p_1)*l(p_2)) \prod_{j=1}^{N_{nsh}} \times P((E_j^1 + E_j^2) \,|\, k(p_1)*l(p_2))\right], \quad (2)$$

where k, l run each for e, π; N_{sh} is the number of modules where the hits are "shared" by the two particles; N_{nsh} the number of modules where the two particles have "non-shared" hits; $P(E_i \,|\, (k(p_1)*l(p_2))$ are the probability densities for the combination of two particles $k(p_1)$ and $l(p_2)$ with momenta p_1 and p_2 to deposit the total energy E_i in the ith straw tube. If, in the jth TRD module, two tracks are associated with different "non-shared" hits, the energy depositions E_j^1 and E_j^2 from these hits are added.

The probability density distributions used in Eq. (2) were obtained by a convolution of the distributions of the energy deposited by corresponding isolated particles (see Fig. 9). The decision on the nature of each of the two particles is made by selecting the hypothesis corresponding to the largest likelihood value among the four $\mathscr{L}_{kl}$. The discrimination between $e(p_1)*\pi(p_2)$ and $\pi(p_1)*e(p_2)$ hypotheses on the basis of "shared" hits is not possible when $p_1 \sim p_2$. In such a case, energy depositions in "non-shared" hits are treated separately

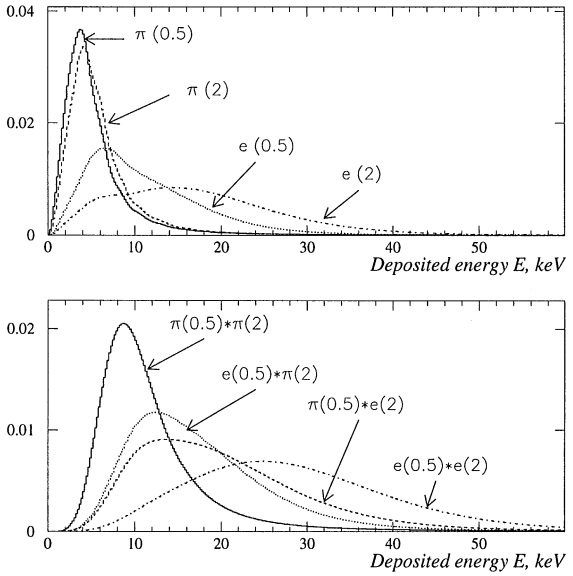

Fig. 9. TRD response to isolated (top) and non-isolated (bottom) 0.5 and 2 GeV/c electrons and pions (Monte Carlo simulation). Particle momentum is shown in brackets.

for each track and provide additional information to help tag the electron or pion.

4.2.2. Monte Carlo tests of the method

The identification procedure for non-isolated particles has been studied for a sample of Monte Carlo events with two tracks generated with a uniform momentum distribution in the range from 0.5 to 50 GeV/c and having 9 "shared" hits in the TRD. The results are presented in Table 1. The expected efficiency of the correct $\pi*\pi$ and e∗e identifications is greater than 90%, with contamination from e∗π and π∗e combinations limited to a few percent. The expected probability to misidentify an e∗e combination as a $\pi*\pi$ pair and vice versa is less than 10^{-3}. On the other hand, a significant fraction ($\sim$25%) of e∗π and π∗e combinations is expected to be identified as an electron pair.

The identification procedures for both isolated and non-isolated particles have also been applied to a sample of Monte Carlo events simulating ν_e CC interactions in the NOMAD detector. The deep inelastic ν_e scattering has been simulated by the LEPTO [10] and JETSET [11] generators,

Table 1
Monte Carlo expectation of the identification efficiency for different combinations of particles sharing 9 hits in the TRD (uniform momentum distribution)

Generated as	Identified as (%)		
	$\pi*\pi$	e∗π,π∗e	e∗e
$\pi*\pi$	91.9	8.1	< 0.1
e∗π,π∗e	0.7	74.8	24.5
e∗e	< 0.1	3.0	97.0

Table 2
Performance of the TRD identification algorithms for non-isolated particles in ν_e CC Monte Carlo simulated events

Generated as	Identified (%) by					
	Isolated particle ID			Non-isolated particle ID		
	$\pi*\pi$	e∗π,π∗e	e∗e	$\pi*\pi$	e∗π,π∗e	e∗e
$\pi*\pi$	0.9	< 0.1	99.1	83.4	15.2	1.4
e∗π,π∗e	1.6	< 0.1	98.4	9.2	38.4	52.4
e∗e	0.1	< 0.1	99.9	3.4	12.6	84.0

while the detector simulation is based on the GEANT [12] package, to which a detailed simulation of the transition radiation emission, the photo-absorption, and the ionization losses in thin gas layers has been added [5]. The results obtained for the identification of particles with more than 3 "shared" hits in $\sim$20 000 generated events are shown in Table 2. The improvement due to the identification algorithm for non-isolated particles is clearly seen. Most importantly, the amount of misidentified $\pi*\pi$ combinations has decreased from $\sim$99% to $\sim$17%.

5. Discussion of the electron identification algorithms

The identification algorithms described in Section 4 demand an accurate measurement of the energy depositions E_i and a precise knowledge of the probability density distributions $P(E_i|\mathrm{e})$ and

$P(E_i \mid \pi)$, i.e., of the detector response to both electrons and pions. In this section, we discuss the impact of the characteristics of incident particles and detector parameters on the energy deposition, the way they were taken into account in the electron identification procedure, and the implementation of the identification algorithm.

5.1. Experimental studies and algorithm assumptions

The response of each straw tube is continuously calibrated by means of ^{55}Fe radioactive sources, emitting 5.89 keV X-rays. The signals from the ^{55}Fe sources allow a precise measurement of the detector response, which varies with the changes in most of the detector parameters (such as high voltage, temperature, pressure, composition of the gas mixture, its H_2O and O_2 contaminations, etc.)

With the sources deposited horizontally in the middle of each detection plane, however, the ^{55}Fe calibration does not take into account possible variations in the gas mixture composition along the straw tubes. An adjustment of the operating conditions has lead to a uniform response of the straw tubes, which is permanently controlled by measurements of the positions of the minimum ionizing peak of muons over the whole detector area [4]. Therefore, in the identification algorithms we assume the response of all 1584 straw tubes to minimum ionizing particles to be identical and independent of the altitude of the particle impact point.

A number of studies have been carried out with the aim of reducing the number of parameters on which the probability density distributions of electrons depend. They have shown that the following parameters can be neglected in the identification procedure.

- *Impact point of the electron.* The transition radiation yield depends on the mean dispersion of the gaps between the foils of the radiator [13] which can vary along the large radiator area because of local inhomogeneities. Consequently, one could expect an X-ray yield dependence of the impact point of the electron on a radiator. A thorough scan of the surface of the radiators by 10 GeV/c electrons in a test beam showed no variation in the X-ray production rate within the 5% accuracy of the measurements.
- *Module position in a doublet.* In the 4 TRD doublets, the second detection plane of a doublet detects about 10% of the X-ray photons emitted in the radiator of the first module which were not absorbed in the first detection plane. Due to this effect, a larger average response of the second module is expected. On the other hand, the regularity of the spacing between the foils was substantially improved during the manufacturing of the radiators. It was decided to install 4 radiators of inferior quality as second radiators of a doublet in order to compensate their lower X-ray yield by a higher detection rate. The signal in the first and second detection planes of a doublet has been studied for a sample of δ electrons from NOMAD data (see Section 6). No difference in the module responses was observed at a level of 3% measurement accuracy.
- *Angle with respect to the radiator.* The angle between the incident particle and the radiator surface could affect the transition radiation yield by changing the distance through the foil and spacing traversed by a particle [14]. The simulation showed a compensation between the increase in the transition radiation production and the increased X-ray photon re-absorption in the radiator in the relevant angular range [5].

Based on these studies we assumed in the implementation of the electron identification algorithms that the probability density distributions both for electrons and pions do not vary from one detection plane to another or over the $2.85 \times 2.85\,\mathrm{m}^2$ surface of the detector and depend only on the Lorentz factor of the incident particle.

5.2. Implementation of the identification algorithms

To study the detector response to electrons and pions, test beam measurements [4] and a detailed simulation of the detector [5] have been performed. Due to the impossibility of in-situ calibration of the entire detector by electron and pion beams, the TRD simulation program that had been checked with test beam measurements was used to compute the probability density distributions of the energy

deposition by isolated and non-isolated particles, taking into account:

- the dependence of ionization losses and transition radiation yield on the Lorentz factor of the incident particle;
- the Auger and fluorescence effects in the process of photo-absorption in xenon [15];
- the mean effect of the cylindrical shape of the straw tubes;
- the space charge corrections for the response of the straw tubes as a function of the energy of the detected photons [4].

To identify isolated particles, the probability density distributions were generated for a set of different momenta of electrons and pions and tabulated. We have also computed and stored the integrated likelihood ratio distributions for electrons and pions (see Fig. 6) as a function of their momenta and number of associated hits. This information allows us to tighten (loosen) electron selection criteria according to the goals of the analyses. By default, a pion rejection factor of 10^3 is required. An interpolation procedure is used to account for the measured momentum of a particle. For the identification of non-isolated particles, only the probability density distributions for the four possible hypotheses were computed and tabulated as a function of the particle momentum.

The performance of the TRD obtained in the analysis of the real data described below confirms the validity of the assumptions, the excellent steering of the detector, and the correct description of the detector response by the simulation program.

6. TRD performance with experimental data

The TRD performance has been studied using experimental data in situ, with the TRD installed as a part of the NOMAD detector. The agreement between the expected and the observed response, as well as the performance of electron identification for isolated particles were tested on two samples of events selected during NOMAD data acquisition:

- muons crossing the detector between two neutrino spills (Section 6.1);
- δ electrons produced by straight-through muons (Section 6.2).

The latter sample has also been used to study the performance of the identification procedure for non-isolated particles (Section 6.3.1). Finally, the electron identification algorithm for non-isolated particles has been applied to electron-positron pairs resulting from photon conversions (Section 6.3.2).

6.1. TRD performance for minimum ionizing particles

A sample of more than 200 000 straight-through isolated muons in the momentum range from 2.5 to 50 GeV/c, recorded during the "flat top" period of the SPS accelerator cycle, has been analysed. Experimental and simulated spectra of the ionization losses of muons in the TRD have been compared for different muon momenta. An excellent agreement between data and simulation was found over 3 orders of magnitude, as shown in Fig. 10 for 10 GeV/c muons.

The TRD identification algorithm for isolated particles was applied to a fraction of the muon sample. The probability for a muon to be identified as an electron was found to be $\varepsilon_\mu = (1.17 \pm 0.30) \times 10^{-3}$, which is in agreement with a required $R = 10^3$ rejection factor. The distribution of the likelihood ratio probability (see Fig. 6) for muons is shown in Fig. 11. The flatness of the histogram confirms the agreement between the input parameters of the identification algorithm and the data. The absence of a peak at low probability values shows also the purity of the selected sample of muons and the absence of electron admixture.

6.2. TRD performance for electrons

As the TRD is an essential tool for electron identification in NOMAD, selecting an unbiased electron sample from neutrino interaction events in order to evaluate the performance of the TRD is

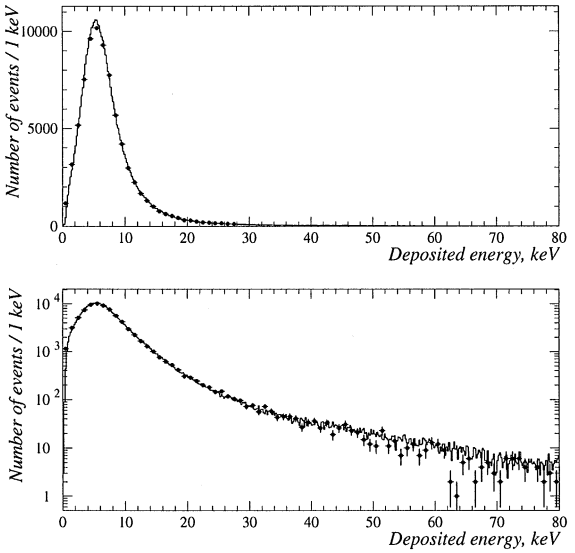

Fig. 10. Comparison of experimental (points with error bars) and simulated (histogram) energy losses of 10 GeV/c muons (linear and logarithmic scales).

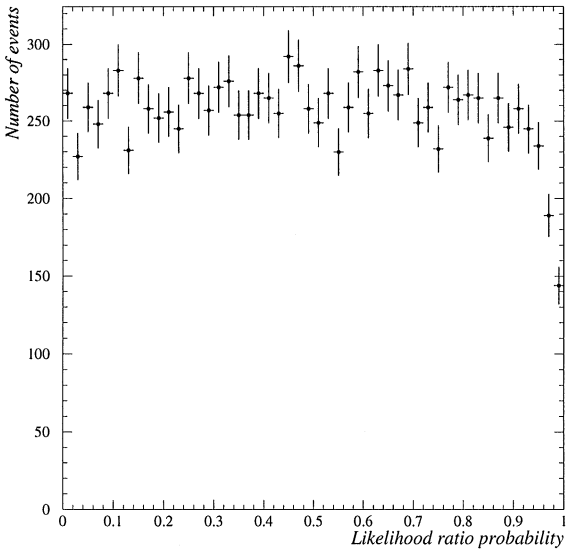

Fig. 11. Distribution of likelihood ratio probability for muons.

problematic. Instead, the in situ detector response to electrons was studied on a sample of δ-rays emitted by "flat top" muons. Such δ electrons are well suited for the studies of TRD performance:

- With an average momentum of the "flat top" muons of about 20 GeV/c, the maximum allowed energy of the emitted δ-ray, $E_\delta^{\max}$, is about 13 GeV [16], well above the TRD identification threshold of 0.5 GeV.
- The angle of emission of a δ-ray electron with energy E_δ is given by the expression [17]:

$$\cos^2\theta = \frac{E_\delta}{E_\delta^{\max}}. \tag{3}$$

Consequently, a large fraction of δ electrons with E_δ of the order of a few GeV is expected to be spatially well separated from the muon track.

The criteria for δ-ray event selection, based only on the topology of the event and the muon identification, are totally independent of the TRD electron identification. A sample of 1216 δ-ray electrons was selected by requiring two track events including a muon (identified in NOMAD muon chambers) and a second particle (δ-ray) with a momentum above 0.5 GeV/c. An example of a selected event is shown in Fig. 12. Fig. 13 shows the momentum distribution of the selected δ-rays which is in agreement with the expected $1/E_\delta^2$ behaviour [16].

The selected sample of δ-rays allows one to compare the simulated and experimental spectra of energy deposited in the TRD by low momentum electrons. Their excellent agreement is shown in Fig. 14. The simulated spectrum was generated by

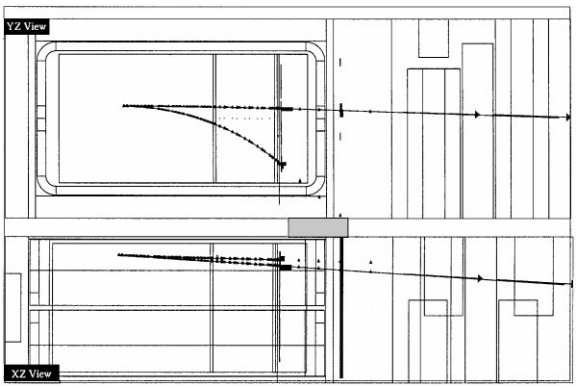

Fig. 12. An example of a δ-ray event. The muon track (observed in the muon chambers) and the δ electron track (absorbed in the electromagnetic calorimeter) are well separated in both projections.

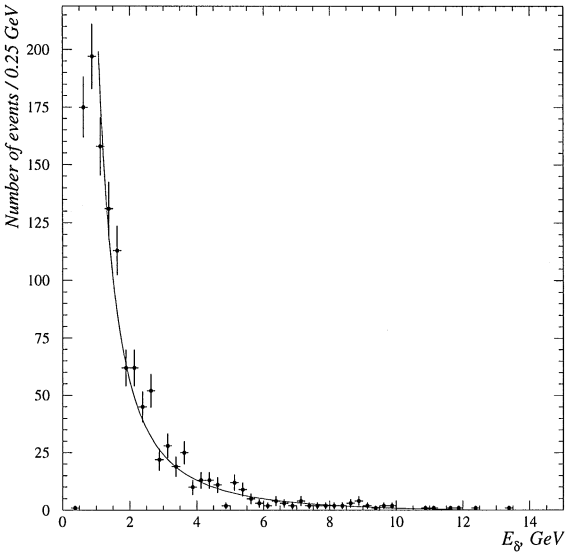

Fig. 13. Momentum distribution of δ-rays. A $1/E_\delta^2$ fit of the momentum distribution is shown.

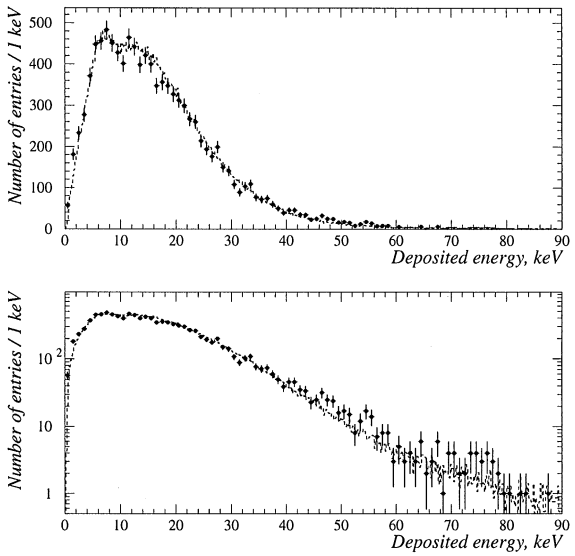

Fig. 14. Comparison of experimental (points with error bars) and simulated (dashed line) distributions of the energy deposited in the TRD by δ electrons (linear and logarithmic scales).

taking into account the measured δ-ray momentum and angular distributions.

The TRD electron identification algorithm for isolated particles, applied to the sample of 1216 δ-rays, has identified 1075 electrons. The measured value of the electron identification efficiency $\varepsilon_e = (88.4 \pm 2.7)\%$ is in agreement with the expected $(89.9 \pm 1.1)\%$ for the identification of electrons at low momenta for a pion rejection factor of 10^3.

6.3. *Performance of the identification of non-isolated particles*

6.3.1. *Sample of δ-ray electrons*

The identification of non-isolated particles has been studied on the sample of muons emitting δ-rays described in Section 6.2. Non-isolated particles were produced from data by adding, plane by plane, the energy deposition of an isolated muon and an isolated electron from two separate events, thus generating 9 "shared" hits. The performance of the identification algorithm on these data and on simulation is shown in Table 3. About 64% of e∗μ combinations are correctly identified.

6.3.2. *Photon conversions*

Another test of the identification of non-isolated particles was performed on photon conversion pairs. The electron and positron resulting from a photon conversion are produced at a small angle with respect to each other and usually lead to "shared" hits in TRD. On the other hand, due to the magnetic field in the detector, the two tracks are opened up in the vertical projection and are reconstructed separately by the drift chambers.

Based on the topology of the conversions and requiring that the invariant mass of a pair be compatible with that of a photon, we selected about 600 electron-positron pairs from a sample of a few thousand ν_μ CC neutrino interaction events

Table 3
The performance of the identification procedure for non-isolated particles applied to the summed energy depositions by muon and δ electron (π∗e combination)

Reconstructed as	Data, %	Simulation, %
π∗π	2.9	1.0
e∗π,π∗e	63.9	72.1
e∗e	33.2	26.9

recorded in NOMAD. Among them, in 75 cases both tracks had a momentum above the identification threshold and more than 3 "shared" hits in the TRD. Of these, 65 pairs were correctly recognized by the identification procedure for non-isolated particles as an e∗e combination. The efficiency obtained, $(86.7 \pm 10.8)\%$, is in agreement with the 86.0% Monte Carlo expectation for the identification of e∗e combinations with the measured momentum distribution.

7. Conclusions

The algorithm developed for the identification of isolated particles in the NOMAD TRD provides a 10^3 pion rejection factor for a 90% electron identification efficiency in the momentum range 1–50 GeV/c. The procedure, designed for the identification of non-isolated particles, significantly reduces the number of mis-identifications, especially in large multiplicity events.

The simulated and the observed detector response, both to minimum ionizing particles and to electrons, are in excellent agreement. The results obtained for muons and electrons during NOMAD data acquisition confirm the assumptions made in the implementation of the identification algorithms.

Acknowledgements

We would like to thank Prof. F. James for discussions concerning the identification algorithms. Part of this work was developed in the framework of the JINR (Dubna)-LAPP (Annecy)-LPNHE (Paris) research network and we gratefully acknowledge the financial support of the French "Ministère de l'Education Nationale, de l'Enseignement Supérieur et de la Recherche". Finally, we are grateful to the CERN and LAPP technical teams for their very competent work in the construction of the NOMAD TRD.

References

[1] NOMAD Collaboration, CERN-SPSLC/91-21 (1991), CERN-SPSLC/91-48 (1991), CERN-SPSLC/91-53 (1991), CERN-SPSLC/93-31 (1993).
[2] The NOMAD Collaboration, The NOMAD Experiment at the CERN SPS, Nucl. Instr. and Meth. A 404 (1998) 56.
[3] M.C. Gonzalez-Garcia, J.J. Gomez-Cadenas, Phys. Rev. D 55 (1997) 1297; B. Van de Vyver, Nucl. Instr. and Meth. A 385 (1997) 91.
[4] G. Bassompierre et al., A large area transition radiation detector for the NOMAD experiment, Nucl. Instr. and Meth. A 403 (1998) 363.
[5] T. Fazio, Le détecteur à rayonnement de transition de l'expérience NOMAD pour l'identification du τ dans le canal $\tau^- \to e^- \bar{\nu}_e \nu_\tau$, Thèse pour obtenir le titre de Docteur de l'Université Joseph Fourier-Grenoble 1.
[6] M. Anfreville et al., Nucl. Instr. and Meth., to be submitted.
[7] G.M. Garibian, JETP 6 (1958) 1079; 10 (1960) 372; K.A. Barsukov, JETP 10 (1960) 787; X. Artru et al., Phys. Rev. D 12 (1975) 1289; L. Durand, Phys. Rev. D 11 (1975) 89.
[8] B. Dolgoshein, Nucl. Instr. and Meth. A 252 (1986) 137; A 326 (1993) 434.
[9] Atomic Data and Nuclear Data Tables, vol. 54, no. 2 (1993).
[10] G. Ingelman, Deep inelastic lepton-nucleon scattering, CERN Program Library, Long Writeup W5046, 1989.
[11] T. Sjöstrand, M. Bengtsson, Jet fragmentation and e^+e^- annihilation, CERN Program Library, Long Writeup W5035, 1993.
[12] R. Brun, F. Carminati, GEANT Detector Description and Simulation Tool, CERN Program Library, Long Writeup W5013, 1993.
[13] G.M. Garibian et al., Nucl. Instr. and Meth. 125 (1975) 133.
[14] G.M. Garibian et al., JETP 6 (1960) 1306; J.C. Ashley, Phys. Rev. 155 (1967) 208.
[15] J.E. Bateman et al., Nucl. Instr. and Meth. 135 (1976) 235.
[16] Particle Data Group, Phys. Rev. D 54 (1) (1994).
[17] F. Sauli, Principles of operation of multiwire proportional and drift chambers, CERN Report 77-09 (1977).